Article

Electromagnetic Interference Cancellation in the Frequency Domain Based on the ASEI-VMD Method

Dongwei Chen [ID], Mengzhe Jin, Jinchao Liu, Weidong Liu and Qingyuan Fang *

Hebei Key Laboratory for Electromagnetic Environmental Effects and Information Processing, Shijiazhuang Tiedao University, Shijiazhuang 050003, China; 1202109030@student.stdu.edu.cn (D.C.); anatman_jin@foxmail.com (M.J.); 1202110008@student.stdu.edu.cn (J.L.); liuwd@stdu.edu.cn (W.L.)
* Correspondence: fangqingyuan@stdu.edu.cn

Abstract: In electromagnetic compatibility (EMC) testing, accurately extracting the radiation emission characteristics from the Equipment Under Test (EUT) in complex electromagnetic environments remains a daunting task. This paper presents a solution by introducing of a frequency-domain electromagnetic interference cancellation method based on the Adaptive Singular Envelope Iterative Variational Mode Decomposition (ASEI-VMD). The process begins with the application of the Adjacent Singular Envelope Entropy Ratio (ASEER) as an evaluation metric to adaptively discern the number of decomposition layers and the penalty factor, allowing the effective decomposition of signals from various channels into modal signals sharing the same center frequency and bandwidth. The singular envelope entropy of each VMD mode is computed as the basis for assessing the efficacy of components in the VMD. This step distinguishes the signals encapsulating the EUT frequency information, which are then isolated for cancellation to retrieve the actual EUT-radiated emission signal. Simulation and experimental data validate the efficacy of this approach. Uniquely, it neither places demands on the testing site nor requires prior conditions for the EUT. The retrieved signal exhibits a correlation of over 96% with the source signal, maintaining a signal-power error below 3 dB. It is suitable for conducting electromagnetic radiation emission testing in complex environments.

Keywords: ASEI-VMD; adjacent singular envelope entropy ratio; electromagnetic interference; frequency-domain cancellation

1. Introduction

System-level electromagnetic radiation testing requires a test site that mimics "free space" as closely as possible within the given environmental limitations. This approach minimizes the potential distortion of measurement results caused by environmental electromagnetic interference. While anechoic chambers offer a controlled testing setting, they present difficulties when testing large-scale, mobile systems (such as vehicles [1], high-speed trains [2], airplanes [3], etc.).

The pursuit of exhaustive and accurate radiation emission data necessitates a comprehensive examination of interference cancellation techniques [4,5] at the testing site. This strategy plays a crucial role in acquiring reliable data and significantly contributes to our understanding of the emission characteristics of electromagnetic radiation. This research highlights the complexity of electromagnetic interference environments and seeks to directly resolve them. Its primary objective is to develop a method for testing electromagnetic radiation emission that can simulate the characteristics of an anechoic system virtually. Notably, this proposed method seeks to produce effective results without requiring prior knowledge of the EUT, thereby expanding its applicability and augmenting its effectiveness.

Adaptive interference cancellation is mainly applied to the interference reduction of sounds [6,7], medical clinical detections [8,9], ship sonars [10–12], and so on. Lu et al. introduced a novel method for the in situ testing of electromagnetic compatibility using a virtual

chamber [13]. The technique, based on spatial domain cancellation, effectively reduced background interference. It surmounted restrictions associated with the count of interferers and eliminated ambiguity from direction-of-arrival (DOA) algorithms. The method is particularly effective for suppressing co-channel and multipath interference, as long as the interference direction differs from that of the EUT. Zhang et al. proposed an interference cancellation algorithm based on the classical Empirical Mode Decomposition (EMD) [14]. It used EMD to decompose multi-frequency signals into multiple single-frequency signals and reconstructed them. Then it used an improved Least Mean Square (LMS) algorithm for interference cancellation to achieve better filtering performance. Liu et al. proposed a novel multi-channel electromagnetic radiation synchronous blind-source separation method that combines Multiple Empirical Mode Decomposition (MEMD) with Independent Component Analysis (ICA) [15]. The approach employed noise-assisted MEMD for the decomposition of multi-channel data and the creation of virtual channels. The Synthetic Screening algorithm filters Intrinsic Mode Functions (IMFs) during decomposition. It conducts Independent Component Analysis (ICA) on the newly derived multi-component input signals, thereby extracting the original electromagnetic radiation source signals and effectively overcoming the limitations of EMD: pattern mixing, multi-channel data handling, and ICA analysis uncertainty. Cakir et al. proposed a technique for mitigating background interference in low-frequency electromagnetic radiation emission testing. The approach entailed continuously fluidizing and recording oscilloscope data in an uninterrupted cycle, thereby preserving phase information without disruption [16]. The oscilloscope data included continuous streams with two adjacent segments: The first segment contained both EUT data and background interference information, while the second segment solely contained the background interference when the EUT is turned off. After gathering all the data, the precise estimation of background interference in the first segment utilized information from the second segment. Knowledge of the phase difference allowed the subtraction of the estimated background interference from the combined EUT and background interference data, resulting in EUT time-domain data. Zhang et al. proposed an adaptive noise spectrum estimation suppression technique [17]. The power-spectrum-estimation correlation method was used to analyze the mixed signals to obtain the frequency point or frequency band where the EUT-radiated emission signal had an obvious peak. Then multiple notch filters were designed according to the obtained frequency and frequency band to realize the suppression of the EUT radiation emission signal component of the reference channel. The limitations of the existing methods primarily manifest in the following facets:

1. The null depth of the antenna array fails to satisfy spatial filtering needs. If the radiation direction of the EUT is not unique, the performance of the electromagnetic radiation emission test will be significantly reduced.
2. The EMD method is prone to modal aliasing, and the suitability conditions for the LMS algorithm are rather idealistic, failing to align with practical testing requirements.
3. The transient nature of the time-domain signal results in a significant disparity in the signals received by the basic two-channel test system, consequently impacting the electromagnetic interference cancellation performance.

The VMD is a technique for decomposing a non-smooth signal into a collection of modal functions, each exhibiting distinct frequency and magnitude characteristics [18–21]. The VMD method has applications in several fields, such as signal processing [22] and mechanical fault diagnosis [23]. Mao et al. utilized the Sparrow Search Algorithm (SSA) to optimize the parameters of VMD to search for the decomposition layer K and the penalty factor α [24]. Li et al. utilized a genetic algorithm to optimize the parameters of the VMD algorithm [25]. The genetic algorithm possesses a rapid global search capability and extensive adaptability and has been widely employed for optimizing various parameters. When the genetic algorithm seeks the optimal decomposition effect of the VMD algorithm, it is necessary to determine a reasonable optimization target. Wang et al. proposed an adaptive VMD method that determines the number of decomposition layers and bandwidths by setting thresholds for the center frequencies between different IMF components [26]. The

disadvantage of the above method is that its iterative execution could be slower, and over-decomposition may occur, thus damaging the stability of the decomposition process. Over-decomposition in the above method can be attributed to the inappropriate setting of the objective function and the simultaneous adjustment of the two parameters. It is impossible to determine which of these two parameters causes the over-decomposition. It cannot distinguish the effective IMF component when there is a component very close to the center frequency of the effective IMF component.

This paper is dedicated to addressing the issue of accurately extracting the EUT's radiated emission signal without prior knowledge about the EUT. A novel approach to extracting the actual radiated emission characteristics of the EUT amidst a complex electromagnetic environment is proposed. The proposed method revolves around utilizing ASEI-VMD for frequency-domain electromagnetic interference cancellation. This method not only resolves the issue of accurately extracting the authentic radiated emission signal from the EUT without prior knowledge but also effectively mitigates the adverse impact of the reference channel, which could be contaminated with the EUT-radiated emission signal, thereby enhancing the algorithm's performance. Simulation and experimental results confirm the method's validity, revealing its adaptability to testing environments without demanding strict conditions. It consistently ensures the accurate retrieval of the actual radiated emission signal from the EUT. The correlation between the canceled EUT-radiated emission signal and the actual EUT-radiated emission signal can surpass 96%, while maintaining a power error of under 3 dB. This method is suitable for conducting electromagnetic radiation emission tests in intricate electromagnetic environments.

2. Theories and Methods

2.1. Traditional VMD Method

The VMD is a non-recursive signal decomposition method that is a sophisticated generalization of the classical Wiener filter, extended to multiple adaptive frequency bands.

The VMD enables the decomposition of a real-valued signal into a predefined number of IMFs. Assume that f represents the decomposed signals. The detected target signal type is, specifically, a narrowband signal. All modes are tightly centered around the central frequency (the criterion for being tightly centered around the center frequency is when the ratio of the decomposition bandwidth to the center frequency is less than or equal to 1), and the bandwidth is estimated by the L_2 norm of the corresponding demodulated signals, which results in the constrained variation problem shown below:

$$\begin{cases} \min_{\{u_k\}\{\omega_k\}} \left\{ \sum_{k=1}^{K} \left\| \partial_t \left[(\delta(t) + \frac{j}{\pi t}) * u_k(t) \right] e^{-j\omega_k t} \right\|_2^2 \right\} \\ \text{s.t.} \sum_{k=1}^{K} u_k = f \end{cases} \tag{1}$$

where $\{u_k\} := \{u_1, u_2, \ldots, u_K\}$ represents the modal signals, $\{\omega_k\} := \{\omega_1, \omega_2, \ldots, \omega_K\}$ denotes the central frequencies of each mode, ∂_t denotes the derivative of a function concerning time t, and $\delta(t)$ denotes the unit pulse function.

To determine the optimal solution for the constrained variation problem, a Lagrange multiplier λ and a penalty factor α are introduced. The augmented Lagrange function expression is given by:

$$L(\{u_k\}, \{\omega_k\}, \{\lambda\}) := \alpha \sum_{k=1}^{K} \left\| \partial_t \left[(\delta(t) + \frac{j}{\pi t}) * u_k(t) \right] e^{-j\omega_k t} \right\|_2^2 + \left\| f(t) - \sum_{k=1}^{K} u_k(t) \right\|_2^2 + \left\{ \lambda(t), f(t) - \sum_{k=1}^{K} u_k(t) \right\} \tag{2}$$

K is designated as the number of decomposition layers, and the frequency-domain IMF expressions are initialized. Following this, the center frequency ω_k^1 and the Lagrange

multiplier $\hat{\lambda}_k$ of IMF $\hat{u}_k^1$ are obtained. The updated formula for the IMF component u_k and its central frequency ω_k is as follows:

$$
\begin{cases}
\hat{u}_k^{n+1} = \dfrac{\hat{f} - \sum_{i<k} \hat{u}_i^{n+1} - \sum_{i>k} \hat{u}_i^n + \frac{\hat{\lambda}^n}{2}}{1 + 2\alpha(\omega - \omega_n^k)^2} \\[4mm]
\omega_k^{n+1} = \dfrac{\int_0^\infty \omega |\hat{u}_k(\omega)|^2 d\omega}{\int_0^\infty |\hat{u}_k(\omega)|^2 d\omega}
\end{cases}
\tag{3}
$$

Following each update of the IMF component and central frequency, the Lagrange multiplier operator is adjusted until the convergence condition is reached. The parameter ε represents the tolerance of the convergence criterion, which is preset as $\varepsilon = 10^{-6}$ in this context.

$$
\begin{cases}
\hat{\lambda}^{n+1} \to \hat{\lambda}^n + \tau(\hat{f} - \sum\limits_{k=1}^K \hat{u}^{n+1}) \\[4mm]
\sum\limits_{k=1}^K \dfrac{\left\| \hat{u}_k^{n+1} - \hat{u}_k^n \right\|_2^2}{\left\| \hat{u}_k^n \right\|_2^2} \leq \varepsilon
\end{cases}
\tag{4}
$$

where τ is the noise tolerance.

The traditional VMD (T-VMD) method encounters difficulties in determining the parameters K and α dynamically during signal processing. Existing adaptive VMD methods still exhibit over-decomposition issues, failing to meet practical requirements.

2.2. ASEI-VMD Method

A novel approach is introduced to adaptively determine the decomposition layer number K and the penalty factor α, offering a solution to the difficulties traditionally encountered in determining these parameters. This method incorporates an iterative VMD framework combined with singular envelope entropy. The chaotic characteristics of different modal signals were used to inform the decision regarding the number of decomposition layers and the decomposition bandwidth. This was achieved by reconstructing the effective components of each modal signal.

Assume that the decomposed IMF components are denoted as $\{u_k\} = \{u_1, u_2, \ldots, u_K\}$, with the length of each modal signal being N. The decomposition process results in the formation of the corresponding Hankel matrix of $m \times n (m \leq n)$.

$$
H_{m\times n} =
\begin{bmatrix}
u(1) & u(2) & \cdots & u(n) \\
u(2) & u(3) & \cdots & u(n+1) \\
\vdots & \cdots & \cdots & \cdots \\
u(m) & u(m+1) & \cdots & u(N)
\end{bmatrix}
\tag{5}
$$

where m represents the number of matrix rows, n is the number of matrix columns, and $N = m + n - 1$. The Hankel matrix undergoes a singular value decomposition [27–29], represented as

$$
H = UEV^T
\tag{6}
$$

where both U and V are orthogonal matrices. The matrix E is an $m \times n$ diagonal matrix by the equation

$$
E =
\begin{bmatrix}
\varepsilon & 0 \\
0 & 0
\end{bmatrix}
\tag{7}
$$

Within this matrix, $\varepsilon = \text{diag}(\lambda_1, \lambda_2, \ldots, \lambda_r)$ is the matrix of singular values for each modal signal. It is specified that $\lambda_1 \geq \lambda_2 \geq \ldots \geq \lambda_r$, and r is the rank of the matrix.

When the first i's effective singular values contain more than 90% of the entire modal signal's information, each modal signal is reconstructed as $u_k' = u_{\lambda_1} + u_{\lambda_2} + u_{\lambda_3} + \cdots + u_{\lambda_i}$. The reconstructed modal signals are denoted as set $\{u_k'\}$.

$$
\{u_k'\} = \{u_1', u_2', \ldots, u_K'\}
\tag{8}
$$

Within the framework of this study, a critical parameter, the singular envelope entropy, is utilized. This measure serves as a metric for quantifying the envelope signal, which is derived subsequent to the Hilbert demodulation operation on the first i's effective components. The envelope signal is obtained after the Hilbert demodulation operation for the first i's effective components. The sparse characteristics and magnitude of the signal both influence the signal complexity. By utilizing the first i's effective components to represent a signal, the interference information provided by irrelevant components is avoided, resulting in accurate identification of signals containing EUT components. The phenomenon of over-decomposition and under-decomposition occurs, which impacts the algorithm's overall performance. Signal envelope entropy is defined as the degree of signal confusion, and its formula is the following:

$$
\begin{cases}
P_j = a(j) \big/ \sum\limits_{j=1}^{n} a(j) \\
D_K(j) = - \sum\limits_{j=1}^{n} P_j log_2(P_j)
\end{cases}
\tag{9}
$$

where $a(j)$ represents the envelope signal extracted from a specific signal $\{u'_k\}$ following the Hilbert demodulation operation. P_j represents the normalized form of $a(j)$, which essentially corresponds to the sequence of probability distributions.

The Minimum Singular Envelope Entropy (*MSEE*) is computed for modal components across various decomposition layers. The ratio of the *MSEE* for the corresponding IMF components between decomposition layers K and $K + 1$ is denoted as the *ASEER*. This *ASEER* metric was subsequently used for evaluation purposes. The formula to calculate *ASEER* is provided below:

$$
ASEER = \frac{\min(D_K(j))}{\min(D_{K+1}(j))}
\tag{10}
$$

Modifying the penalty factor (α) and the number of decomposition layers (K) influences the augmented Lagrange function's structure and optimization process. The penalty factor α controls the regularization term's magnitude, affecting sparsity in signal decomposition. Higher α values lead to sparser decomposition, reducing the number of modes and enhancing accuracy. The K value determines the decomposition depth, with higher values providing more detailed decomposition and improved signal representation. This study focuses on the *MSEE*, guiding the selection of optimal K and α, and the *ASEER* is employed as the objective function for the iteration cutoff. The process ensures the sparsity and accuracy of modes containing EUT-radiated emission information, adhering to augmented Lagrange function constraints.

During the iterative process, the initial setting of the penalty factor is typically relatively small. Generally, the value range is within 300~500. After conducting numerous experiments and by referring to [26], it was observed that increasing the penalty factor α significantly enhances the decomposition performance, and the penalty factor performs well when in the order of thousands. When the increment per iteration remains below 100, it becomes challenging to discern notable changes in the decomposition result, potentially leading to an escalation in the complexity of the decomposition process. A setting above 100 results in a slightly larger increment, making it challenging to determine the optimal penalty factor accurately. Therefore, this article chooses a penalty factor increment of 100 for each iteration.

In the process of determining the optimal number of decomposition layers K, the computation of minimum envelope entropy is computed for each iteration step. When $ASEER \leq 1$ is observed, this signifies the occurrence of over-decomposition. This prompts the termination of the iteration process, and the number of decomposition layers is finalized as K. Determine that the number of decomposition layers is unchanged and increase the penalty factor α. When $ASEER \leq 1$ is encountered following n iterations, the iteration concludes. At this juncture, the penalty factor is established as α.

These are the specific decomposition steps for ASEI-VMD:

Step 1: Commence by establishing the initial decomposition layer, denoted as K. Define the default penalty factor, denoted by α, and simultaneously establish the permissible range of values for K.

Step 2: Execute the decomposition process using the initial value, calculate the *MSEE* values for both scenarios where the decomposition layers are K and $K + 1$, and then assess whether the condition $ASEER \leq 1$ holds.

Step 3: When the condition $ASEER \leq 1$ is fulfilled, signifying $D_K < D_{K+1}$, it results in the MSEE of the decomposition layer $K + 1$ being higher than that of K. This suggests that the increase in sparsity corresponds to a rise in *SMEE*, indicating either an over-decomposition of effective components or a decomposition of irrelevant components. The iteration concludes. When $ASEER \leq 1$ is not satisfied, K is incremented by 1, prompting the continuation of the iterative optimization search process.

Step 4: Continuously iterate through steps 2 to 3 until the $ASEER \leq 1$ condition is fulfilled. At this juncture, the corresponding count of decomposition layers K denotes the optimal configuration for decomposition.

Step 5: While keeping the optimal number of decomposition layers K unchanged, an iterative process is initiated for the penalty factor A. A is incremented by 100 for each iteration.

Step 6: If $ASEER \leq 1$, that is, $D_\alpha < D_{\alpha+1}$, this indicates that the *MSEE* for the penalty factor $\alpha + 100$ is greater than that for α. At this stage, the iteration concludes, and the optimal penalty factor is established as α. Otherwise, α is incremented by 100, prompting the continuation of the iterative optimization search process.

Step 7: Continue iterating through steps 5 to 6 until the condition $ASEER \leq 1$ is met, ultimately determining the optimal penalty factor, denoted as α.

Step 8: At the end of the optimization search, the number of decomposition layers K and the penalty factor α are output.

The detailed iteration process is shown in Figure 1.

2.3. Electromagnetic Interference Cancellation Method

After identifying the IMF components containing the actual radiated emission information from the EUT, in scenarios where the signal-to-interference ratio (SIR) is relatively low, the actual EUT-radiated emission signal becomes submerged by environmental interference within the IMF. The modal signal carrying EUT-radiated emission information may include many interference signals, adversely impacting the algorithm's accuracy. Therefore, a cancellation method is implemented to mitigate the effects of interference. Figure 2 below shows the block diagram of the frequency-domain electromagnetic interference cancellation work. Antenna A mainly collects EUT-radiated emission signals and environmental electromagnetic interference, and Antenna B only contains environmental electromagnetic interference. In theory, antenna B exclusively captures environmental electromagnetic interference, and the environmental electromagnetic interference collected by antenna B is identical to that of antenna A. The EUT-radiated emission signal is obtained using the spectral subtraction method (SSM).

However, in practical engineering applications, the interference collected by antenna B will inevitably be mixed with EUT-radiated emission signals. There are significant differences in the amplitude of environmental electromagnetic interference collected by the two antennas. Simple SSM cannot obtain the accurate EUT-radiated emission signal. To guarantee that the EMC testing setup achieves a minimum of a 20 dB reduction in the received radiated emission signal at antenna B compared with antenna A, the separation between antenna B and the transmitting antenna of the EUT is at least ten times greater than between antenna A and the EUT transmitting antenna. This arrangement ensures that the radiation emission signal from the EUT undergoes substantial spatial scattering and attenuation before being detected by the reference-channel signal sensor. In this configuration, the system does not engage in any specific processing of the signals collected

by its primary and reference channels. Antenna A, antenna B, and the EUT-radiating antenna are in the same horizontal straight line. Initially, the number of decomposition layers K and the penalty factor α are determined through an adaptive iterative process based on singular envelope entropy. Subsequently, the two-channel signals are decomposed into mode signals with equivalent center frequencies and bandwidths. The EUT-radiated emission information component corresponds to the lowest singular envelope entropy. Following the fitting of the modal signals containing EUT frequency information in the two channels using the backpropagation neural network (BPNN), a notch-cancellation process is executed to extract the actual radiated emission signal of the EUT.
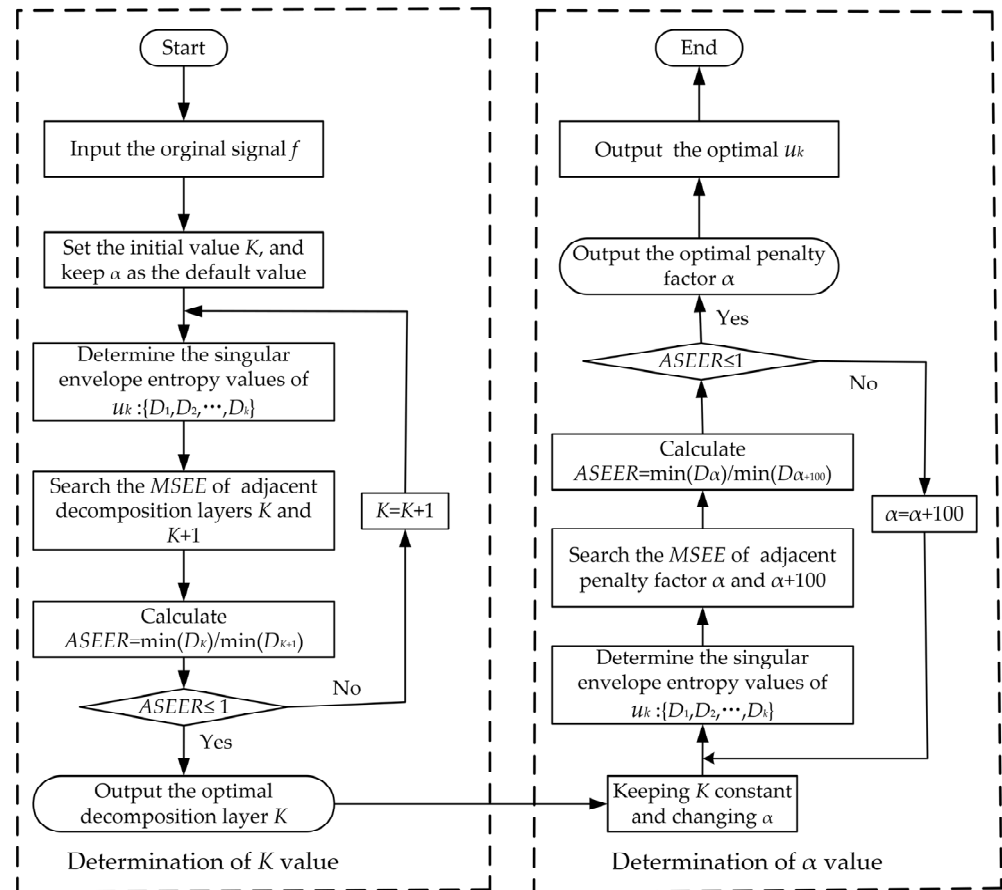
Figure 1. The process of VMD with adaptive singular envelope iteration.
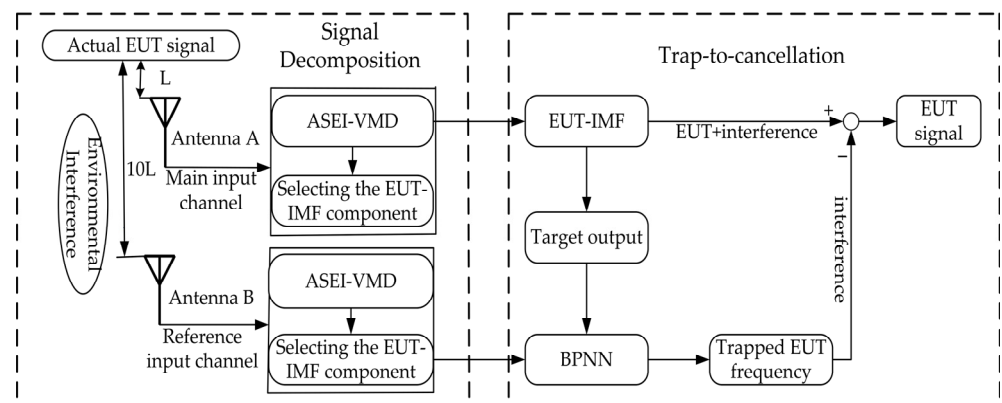
Figure 2. Block diagram of the electromagnetic interference cancellation work in the frequency domain.

The function of the BPNN is mainly to fit the modal signals containing EUT radiation emission information in antennas A and B, so that their electromagnetic interference tends to be the same. BPNN utilizes a single hidden layer comprising 10 nodes, while the input and output layers each consist of a single node. The training set input is the modal component containing EUT information in antenna B, accounting for 75%. The training set output is the modal component containing EUT information in antenna A, accounting for 75%. The test set input is the component containing EUT information in antenna B, accounting for 25%. The test set output is the component containing EUT information in antenna A, accounting for 25%.

Adaptive VMD decomposes the signals from antenna A to obtain the modal signals, which are represented by

$$S_k^A(n) = [u_1^A(n), u_2^A(n), \ldots, u_K^A(n)] \tag{11}$$

Its center frequency set is expressed as:

$$\varphi_k = [\lambda_1, \lambda_2, \ldots, \lambda_K] \tag{12}$$

The estimation of the corresponding decomposition bandwidth is given by

$$\Lambda_k = [\phi_1, \phi_2, \ldots, \phi_K] \tag{13}$$

Antenna B contains the same frequency information as antenna A; only the difference in amplitude is obvious.

It uses the center frequencies ϕ_k and decomposition bandwidths Λ_k in antenna A to equally decompose antenna B's signals, and each mode signal is recorded as

$$S_k^B(n) = [u_1^B(n), u_2^B(n), \ldots, u_K^B(n)] \tag{14}$$

Each of the modal signals in antennas A and B are reconstructed by the first $i's$ singular components. Subsequently, they are transformed into the frequency domain using FFT, and the resulting signal is as follows:

$$\begin{cases} F_k^A(\omega) = [F_1^A(\omega), F_2^A(\omega), \ldots, F_K^A(\omega)] \\ F_k^B(\omega) = [F_1^B(\omega), F_2^B(\omega), \ldots, F_K^B(\omega)] \end{cases} \tag{15}$$

The singular envelope entropy for $F_k^A(\omega)$ is computed, and the modal signals with the lowest singular envelope entropy are the effective components containing the EUT-radiated emission information. Since the two signals are decomposed by same rules, which are based on the same center frequency and decomposition bandwidth, by utilizing the identified modal component containing the EUT information in antenna A as a reference, we can determine the corresponding one containing the EUT information in antenna B.

It is assumed that the IMF component of the EUT-radiated emission signal obtained by the main input channel after VMD is

$$F_1^A(\omega) = S_1^A(\omega) + N_1^A(\omega) \tag{16}$$

The reference channel contains the IMF component of the EUT emission signal as

$$F_1^B(\omega) = \mu S_1^A(\omega) + \beta N_1^A(\omega) \tag{17}$$

in which μ, β ($\mu, \beta \neq 1$) are the amplitude coefficients of the EUT signal and the interference.

To cancel the $\mu S_1^A(\omega)$ component from $F_1^B(\omega)$, a notch filter is introduced. A notch filter is capable of suppressing a specific frequency point or frequency band. The precise transfer function of the notch filter is depicted below:

$$G(s) = \frac{s^2 + \omega_c^2}{s^2 + \omega_{b\omega}s + \omega_c^2} \qquad (18)$$

where $\omega_{b\omega}$ is the trap width, and ω_c is the central frequency of the trap.

After ASEI-VMD, the modal component housing the EUT radiation emission information in antenna A may exhibit traces of interference; however, the frequency information associated with the EUT becomes conspicuously discernible. The cancellation method in this paper takes $F_1^A(\omega)$ as the objective function, and uses $F_1^B(\omega)$ to fit $F_1^A(\omega)$, such that $F_1^B(\omega)$ tends to be equal to $F_1^A(\omega)$. The EUT-radiated emission signal component $\mu S_1^A(\omega)$ in $F_1^B(\omega)$ is suppressed by using the trap (18), and the actual EUT-radiated emission signal is obtained after subtraction.

3. Simulation Analysis

The simulation analysis of the method in this paper is carried out on the MATLAB platform. The reference channel will inevitably be mixed with the EUT-radiated emission signal in the actual electromagnetic environment. The mixed EUT radiation signal varies with the intensity of the EUT emission, and some studies did not specify the processing method. Moreover, the background interference intensity varies between the two channels. When the mixed EUT-radiated emission signal reaches a significant magnitude, the EUT-radiated emission signal after the cancellation may diminish, thereby impacting the effectiveness of the interference-cancellation algorithm. The signal settings used for the simulation validation of the method in this paper were described as

$$
\begin{cases}
S_0 = 0.004\sin(2\pi f_0 t) \\[2mm]
S_1 = exp(-2log2(t - t_0)^2/sigma^2)cos(2\pi freqs(t - t_0)) \\[2mm]
S_A = S_0 + \sum\limits_{j=1}^{4} A_{1j}\sin(2\pi f_j t) + \sqrt{\left(\sum\limits_{j=1}^{4} A_{1j}sin(2\pi f_j t)\right)^2/SNR * randn(1, N)} + 0.1S_1 \\[4mm]
S_B = \eta S_0 + \sum\limits_{j=1}^{4} A_{2j}\sin(2\pi f_j t) + \sqrt{\left(\sum\limits_{j=1}^{4} A_{2j}\sin(2\pi f_j t)\right)^2/SNR * randn(1, N)} + 0.08S_1
\end{cases}
\qquad (19)
$$

where $j = 1, 2, \ldots, 4$; A_{1j} = 0.002, 0.001, 0.001, 0.001; A_{2j} = 0.002, 0.001, 0.002, 0.0015; and SNR = -1 dB. N is the sampling point. The term "freqs" refers to the sampling frequency. The simulated EUT-radiated emission signal frequency is f_0 = 800 MHz, and the simulated electromagnetic interference signals are f_1 = 1.2 GHz, f_2 = 100 MHz, f_3 = 500 MHz, f_4 = 900 MHz, and t = max $(t)/2$. S_1 represents the broadband interference signal. The background interference strength varies between antennas A and B. η is the mixing coefficient (η = 0.5). The standard deviation, denoted as "sigma", has a value of 8×10^{-15}.

3.1. ASEI-VMD Performance Analysis

Signal decomposition is the crucial step in determining the performance of electromagnetic-interference cancellation. Without prior knowledge, the acquired signals undergo decomposition into designated IMF components, within which the actual radiated emission signal from the EUT can be entirely preserved in a single IMF component. The efficient information components are chosen based on the values of each IMF component's singular envelope entropy. The residual components are disregarded in the analysis. ASEI-VMD's performance is validated using simulated signals from channel A. The performance simulation comparison between ASEI-VMD and the Local Mean Decomposition (LMD) [30], Ensemble Empirical Mode Decomposition (EEMD) [31], T-VMD, SSA-VMD, GA-VMD-SVD algorithms in this paper are shown below.

When a signal contains multiple components with similar frequencies or closely spaced frequencies, the signal components from different modes or frequencies merge, making it difficult to separate or distinguish them accurately. This phenomenon is known as modal

aliasing. The over-decomposition phenomenon refers to the situation where the expected EUT-radiated emission signal is decomposed into two or more modal components. The ideal outcome is to have the expected signal decompose into only one modal component.

Figure 3 above displays the modal components containing radiated emission information from the EUT, decomposed by different methods. Analyzing Figure 3a–g above, it is evident that both LMD, GA-VMD-SVD, and EEMD exhibit over-decomposition phenomena, thereby failing to accurately decompose the actual EUT-radiated emission signal into an IMF component. Determining the number of decomposition layers and the penalty factors in T-VMD relies on human experience, which fails to achieve the desired adaptability. The number of decomposition layers and penalty factors in SSA-VMD are determined through an intelligent algorithm that autonomously searches and optimizes these parameters. With an increase in the number of iterations, there is a corresponding rise in running time and computational complexity, subsequently impacting the overall algorithm performance. The method presented in this paper enhances decomposition accuracy and reduces computational complexity while ensuring self-adaptation.
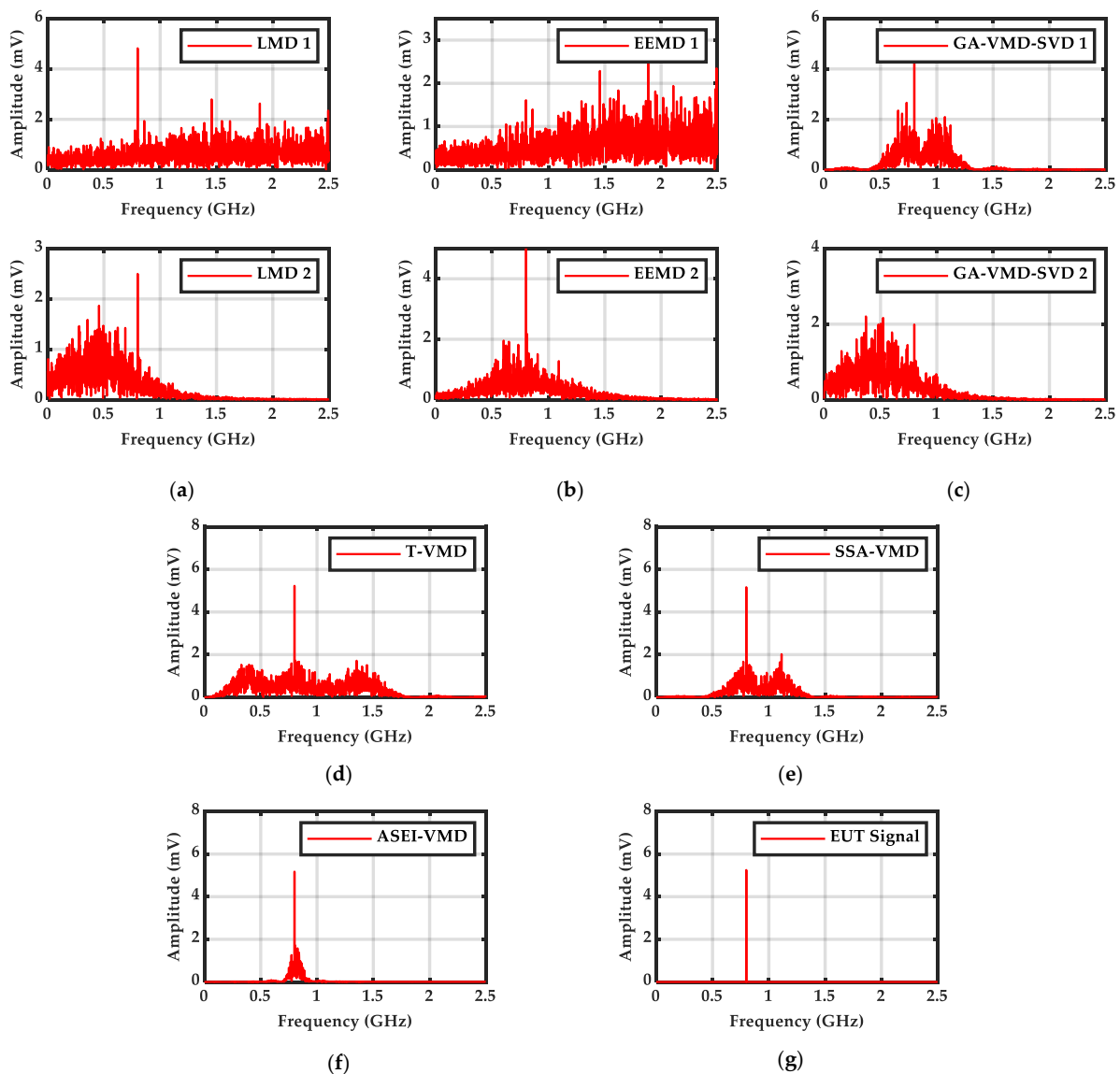
Figure 3. Comparison of the results of different decomposition methods: (**a**) the LMD; (**b**) the EEMD; (**c**) the GA-VMD-SVD; (**d**) the T-VMD; (**e**) the SSA-VMD; (**f**) the ASEI-VMD; (**g**) the actual EUT-radiated emission signal.

3.2. Simulation Analysis of the Frequency-Domain Electromagnetic Interference Cancellation Method

The simulated signals received from antennas A and B correspond to Equation (19). Notably, there exists a disparity in the background interference levels for these two antennas. Furthermore, antenna B is intertwined with the radiated emission signal from the EUT. The signal configurations for the simulation should consider these factors. Figure 4 compares the received signals for the two channels in the simulation. Figure 4a simulates the signals received by antenna A. Figure 4b simulates the signals received by antenna B.

(a)　　　　　　　　　　　　　　　　　　　　　　　　　　　　(b)
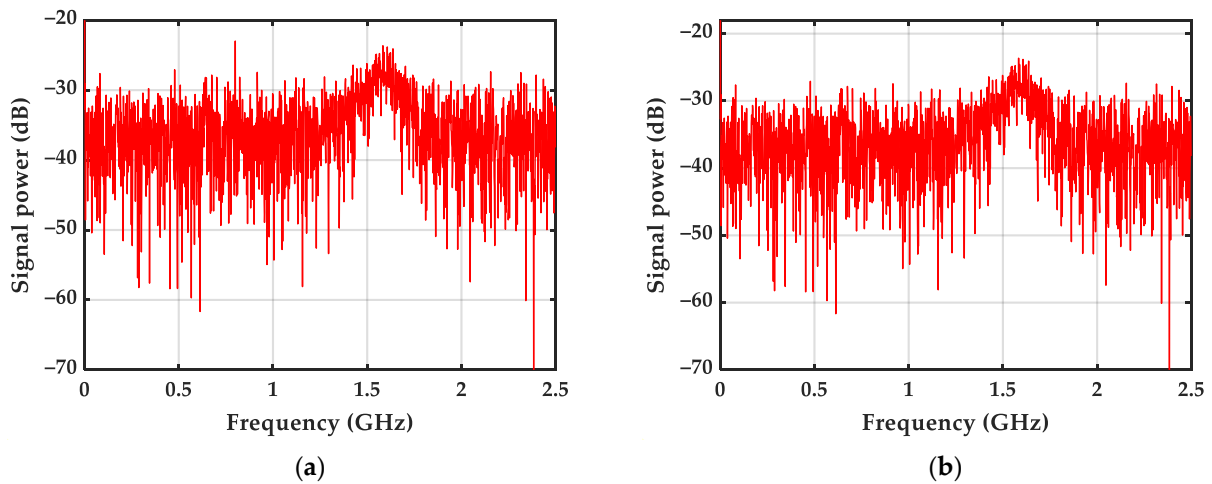
Figure 4. Simulation comparison of received signals: (**a**) from antenna A; (**b**) from antenna B.

Figure 5a compared the EUT-radiated emission power errors obtained under different SIRs in the simulation. The simulation is designed to account for varying EUT radiation and interference intensities during each iteration, thereby assessing the algorithm's cancellation performance under dynamic conditions. It can be seen from the figure analysis that the errors between the actual EUT-radiated emission signal obtained by the algorithm in this paper and the canceled EUT-radiated emission signal can be stabilized below 3 dB under different SIR environments, which meets the actual requirements.

(a)　　　　　　　　　　　　　　　　　　　　　　　　　　　　(b)
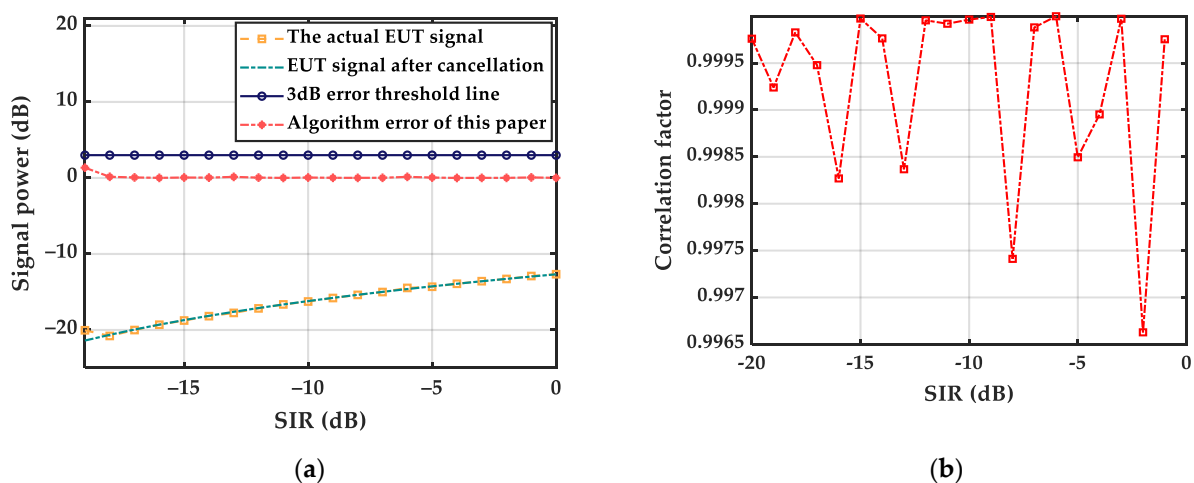
Figure 5. Results of the power errors and the correlation between the EUT-radiated emission signal after cancellation and the actual EUT-radiated emission signal obtained at different SIRs in the simulation: (**a**) the comparison of power errors; (**b**) the comparison of correlation.

To validate the cancellation performance of the algorithm in the simulation, the correlation coefficient (R) is introduced to characterize the amount of interference contained

in the EUT-radiated emission signal after interference cancellation. When the correlation number R is close to 1, the correlation between the EUT-radiated emission signal after cancellation and the actual EUT-radiated emission signal is high, and the interference is negligible. Conversely, a correlation coefficient approaching 0 indicates weak correlation and significant interference. The specific computational formula is as shown:

$$R = \frac{\sum\limits_{i=1}^{N} (x(i) - \overline{x})(y(i) - \overline{y})}{\sqrt{\sum\limits_{i=1}^{N} (x(i) - \overline{x})^2 \sum\limits_{i=1}^{N} (y(i) - \overline{y})^2}} \tag{20}$$

where $\overline{x}$ and $\overline{y}$ are the overall mean values, and x and y are two columns of signal data.

Figure 5b described the correlation between the EUT-radiated emission signal obtained under different SIRs and the actual EUT-radiated emission signal in the simulation. It can be seen from the analysis in the figure that under different SIR environments, the correlation number between the actual EUT-radiated emission signal and the EUT-radiated emission signal obtained by the algorithm in this paper is close to 1, which means that the EUT-radiated emission after the algorithm is canceled, and the signal contains very little interference.

The method presented in this paper is also applicable to testing broadband EUT-radiated emissions. The following section provides verification for such tests. The simulation signal parameters for antennas A and B are as follows:

$$
\begin{cases}
S_0 = 0.1 exp(-2log2(t - t_0)^2 / sigma^2) cos(2\pi freqs(t - t_0)) \\[2mm]
S_1 = \sum\limits_{n=-\infty}^{\infty} rect\left(\frac{t-nT}{\sigma}\right), rect\left(\frac{t-nT}{\sigma}\right) = \begin{cases} 1, \left|\frac{t-nT}{\sigma}\right| \leq 0.5 \\[2mm] 0, \left|\frac{t-nT}{\sigma}\right| > 0.5 \end{cases} \\[4mm]
S_A = S_0 + S_1 + \sum\limits_{j=1}^{3} A_{1j} \sin(2\pi f_j t) + \sqrt{\left(\sum\limits_{j=1}^{3} A_{1j} \sin(2\pi f_j t)\right)^2 / SNR * randn(1, N)} \\[4mm]
S_B = 0.1 S_0 + 0.9 S_1 + \sum\limits_{j=1}^{3} A_{2j} \sin(2\pi f_j t) + \sqrt{\left(\sum\limits_{j=1}^{3} A_{2j} \sin(2\pi f_j t)\right)^2 / SNR * randn(1, N)}
\end{cases} \tag{21}
$$

where $j = 1, 2, 3$; $A_{1j} = 0.002, 0.001, 0.001$; $A_{2j} = 0.002, 0.002, 0.0015$; and SNR $= -5$ dB. The background interference strength varies between antennas A and B. N is the sampling point, T is the pulse period ($T = 0.25$), and σ is the pulse width ($\sigma = 0.1$). The term "freqs" is the sampling frequency. The simulated EUT-radiated emission signal is S_0, and the simulated electromagnetic-interference signals are $f_1 = 100$ MHz, $f_2 = 500$ MHz, $f_3 = 900$ MHz, S_1, and $t = \max(t)/2$. The standard deviation, denoted as "sigma", has a value of 8×10^{-15}.

Figure 6 showed the received signals for the two channels in the simulation. Figure 6a simulates the signals received by antenna A. Figure 6b simulates the signals received by antenna B.

Figure 7a compared the actual EUT-radiated emission signal with the EUT-radiated emission signal after cancellation in the simulation. Electromagnetic interference in the EUT-radiated emission signal after cancellation is minimal, resembling the actual EUT-radiated emission signal. This observation corroborates the algorithm's efficacy.
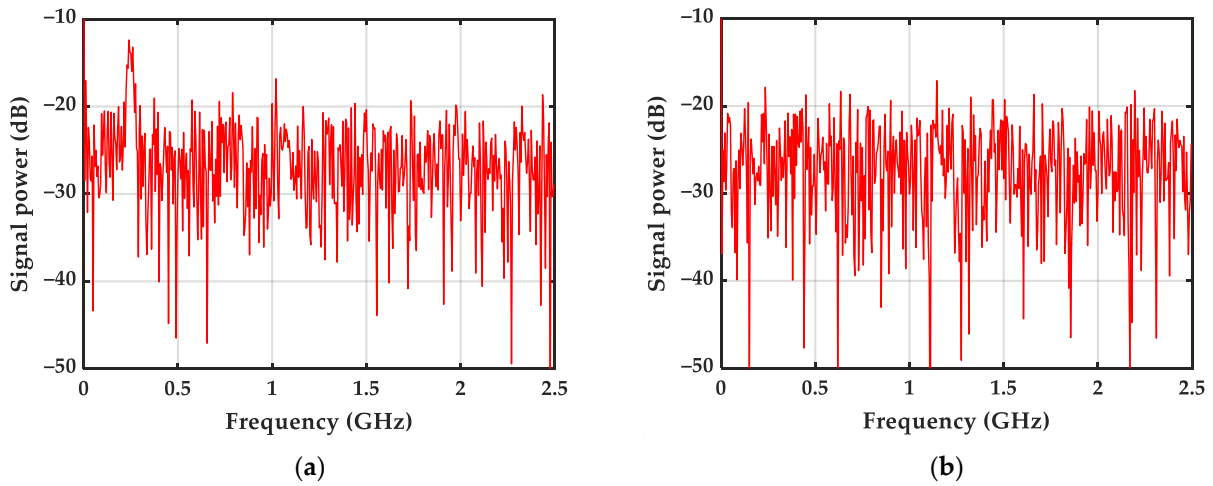
Figure 6. Simulation comparison of the two-channel received signals: (**a**) simulated received signal of antenna A; (**b**) simulated received signal of antenna B.
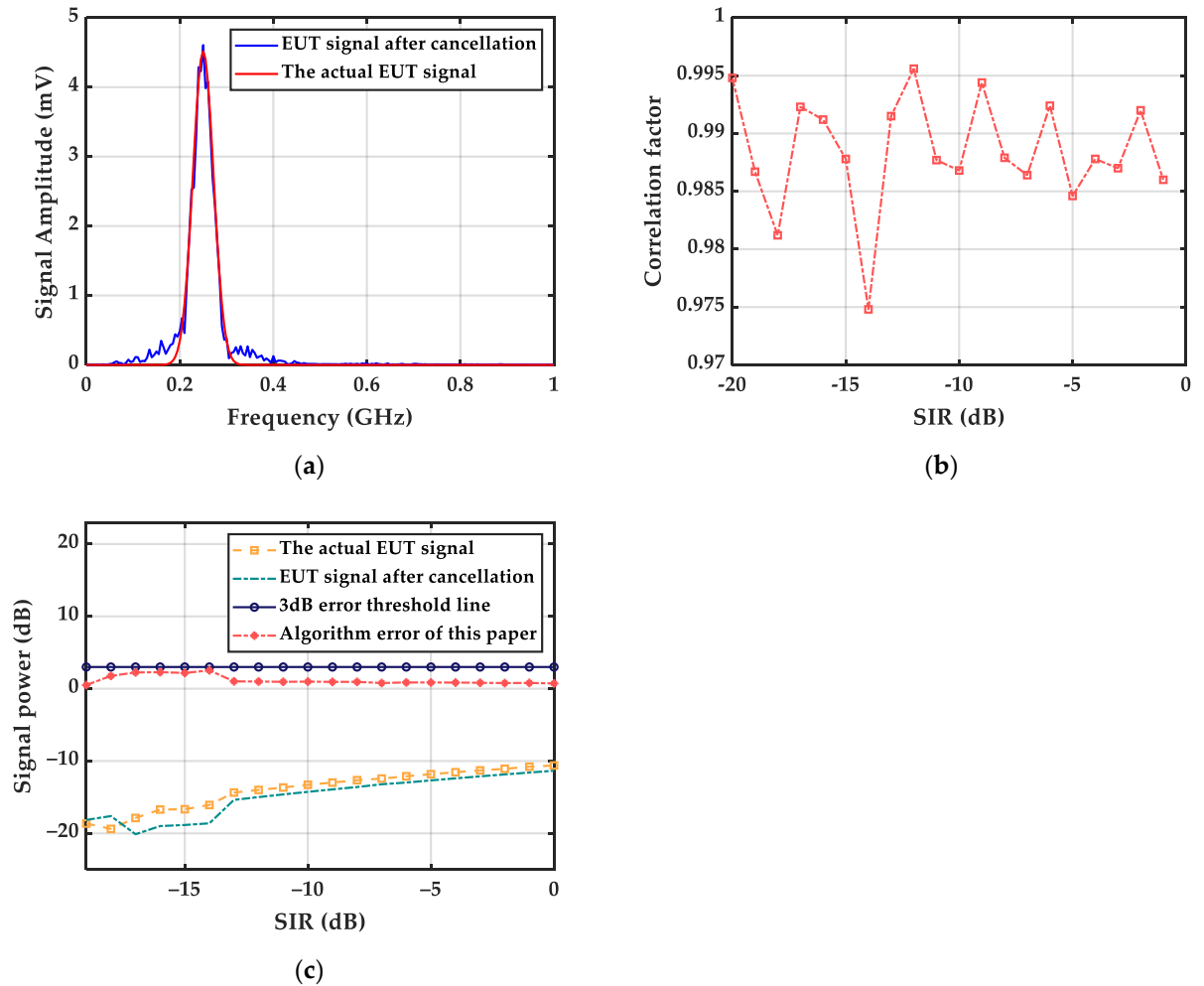
Figure 7. Test results of broadband EUT-radiated emission signals in the simulation: (**a**) output signals after cancellation; (**b**) the comparison of correlation; (**c**) the comparison of power errors.

Figure 7b exhibits the correlation between the EUT-radiated emission signal obtained under different SIRs and the actual EUT-radiated emission signal in the simulation. It can be seen from the analysis in the figure that under different SIR environments, the correlation

between the actual EUT-radiated emission signal and the signal obtained through this algorithm consistently exceeds 97%. The broadband EUT-radiated emission acquired after cancellation satisfies the correlation criteria.

Figure 7c describes the EUT-radiated emission power errors obtained under different SIRs in the simulation. It can be seen from the figure analysis that the errors between the actual EUT-radiated emission signal obtained by the algorithm in this paper and the canceled EUT-radiated emission signal can be stabilized to below 3 dB under different SIR environments, which meets the actual requirements. The simulation analysis above substantiates that the method presented in this article also applies to broadband EUT electromagnetic radiation emission testing.

4. Experimental Verification

Experiments were carried out to verify the method of this paper. Figure 8a illustrates an experimental test in an open environment. Antenna A serves the purpose of capturing both the radiated emission signal from the EUT and the environmental electromagnetic interference. Antenna B is exclusively tasked with capturing the ambient electromagnetic interference present in the environment. The employed transmitting antenna for the EUT is a hybrid logarithmic periodic antenna, specifically the Model 3142E, characterized by a bandwidth from 30 MHz to 6 GHz. The signal generator Model is 1435D, covering a frequency range from 9 KHz to 6 GHz and capable of a maximum output power of 20 dBm. The electromagnetic signal from the EUT is transmitted through the hybrid log–periodic antenna by the signal generator, operating in a continuous cycling signal-emission mode. The receiving device is two self-developed Vivaldi miniaturized antennas with exact specifications. These Vivaldi antennas operate within the frequency range from 0.47 GHz to 12 GHz and provide a gain ranging from 1 dBi to 11 dBi. The distance between antenna A and the EUT-emitting antenna is denoted as L, and the spread between antenna B and antenna A is 9L. This paper employs values of L of 0.5 m and 1 m to validate the algorithm's performance. Data acquisition is facilitated by a four-channel oscilloscope, MSO8104, with a test bandwidth of 2 GHz and a signal-sampling frequency of 10 GHz. The experimental testing location is an open space with no stringent site requirements.

(**a**)   (**b**)
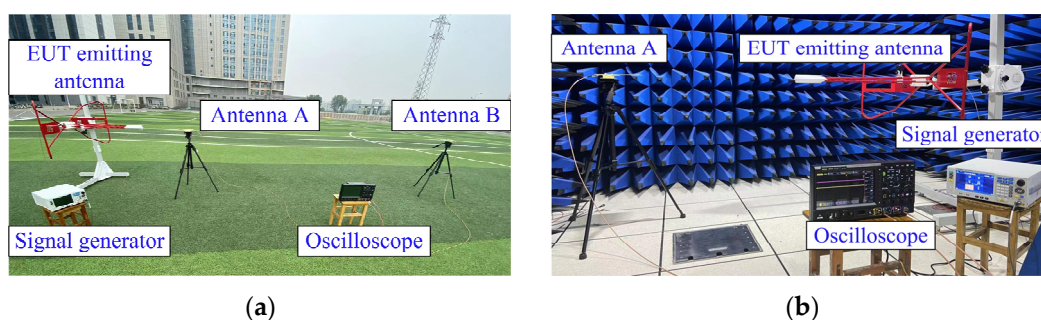
Figure 8. Verification experiment diagram of the cancellation algorithm: (**a**) the open space; (**b**) the anechoic chamber.

Accurate acquisition of actual EUT-radiated emission data is necessary to verify the algorithm's performance. Figure 8b shows the test of the actual EUT-radiated emission signal in an anechoic chamber. It is important to uphold a uniform layout for both the field-test antenna A and the EUT-emitting antenna and to guarantee that the testing of the actual EUT-radiated emission signal remains free from interference by external signals. The actual EUT-radiated emission powers are tested under different signal-emitting powers and distances and compared to determine whether the EUT-radiated emission signal obtained by the algorithm in this paper meets the requirements.

4.1. ASEI-VMD Performance Analysis

The ASEI-VMD method is employed to analyze the measured signals. The transmitting antenna of the EUT transmits a sinusoidal signal characterized by a frequency of 800 MHz and a power level of 0 dB. The decomposition outcomes are presented in the figure below.

By analyzing Figure 9a–g, it can be clearly seen that for the measured signals, not only do the LMD, GA-VMD-SVD, and EEMD methods show over-decomposition, but SSA-VMD and T-VMD also show this over-decomposition phenomenon. The reason for this could be attributed to the improper parameter settings in the T-VMD, where the values of the number of decomposition layers K and the penalty factor α might be either too large or too small, thereby influencing the signal decomposition outcomes. As for the over-decomposition in SSA-VMD, this could be related to the simultaneous adjustment of both the K and α values. During the iterative search for optimal values, these two parameters increase synchronously, leading to an over-decomposition phenomenon. Hence, this paper employs an iterative optimization approach, firstly determining the number of decomposition layers K and then determining the penalty factor α. The effectiveness of the algorithm presented in this paper is confirmed by the precise extraction of the IMF component containing the entire EUT-radiated emission signal, as evidenced in Figure 9f.

Table 1 above shows the performance comparison of the different decomposition methods. Compared with LMD and EEMD, the ASEI-VMD method avoids the phenomenon of modal aliasing and over-decomposition. It also decomposes the actual EUT-radiated emission signal into an IMF component, which meets the requirements of experimental research. In contrast to T-VMD, the adaptive determination of the number of decomposition layers K and the penalty factor α is a notable feature. In contrast to GA-VMD-SVD, this method circumvents the issue of over-decomposition and substantially reduces computational complexity. Compared with SSA-VMD, this approach exhibits significantly reduced computational complexity and improved decomposition stability.

Table 1. Performance comparison of different decomposition methods.

Decomposition Method	Type of Decomposition	Problem Phenomenon	Time Consumption/s	K, α
LMD [30]	Adaptive	Over-decomposition; Modal aliasing	2.18	$K = 6$
EEMD [31]	Adaptive	Over-decomposition; Modal aliasing	7.9	$K = 8$
SSA-VMD [24]	Adaptive	Over-decomposition, EUT information loss	173.36	$K = 9, \alpha = 900$
T-VMD [18]	Artificial experience sets the value of K, α	Over-decomposition, EUT information loss	9.4	$K = 9, \alpha = 700$
GA-VMD-SVD [22]	Adaptive	Over-decomposition, EUT information loss	524.36	$K = 11, \alpha = 1050$
ASEI-VMD	Adaptive, first determine K, then determine the value of α	\	59.4	$K = 14, \alpha = 1900$

Based on the analysis of Figure 10, it is evident that ASEI-VMD does not exhibit an over-decomposition phenomenon. The information of EUT-radiated emission is separately decomposed into an IMF component, and the obtained EUT-radiated emission power is very close to the actual EUT-radiated emission power. This validates the effectiveness of the proposed method in this paper.
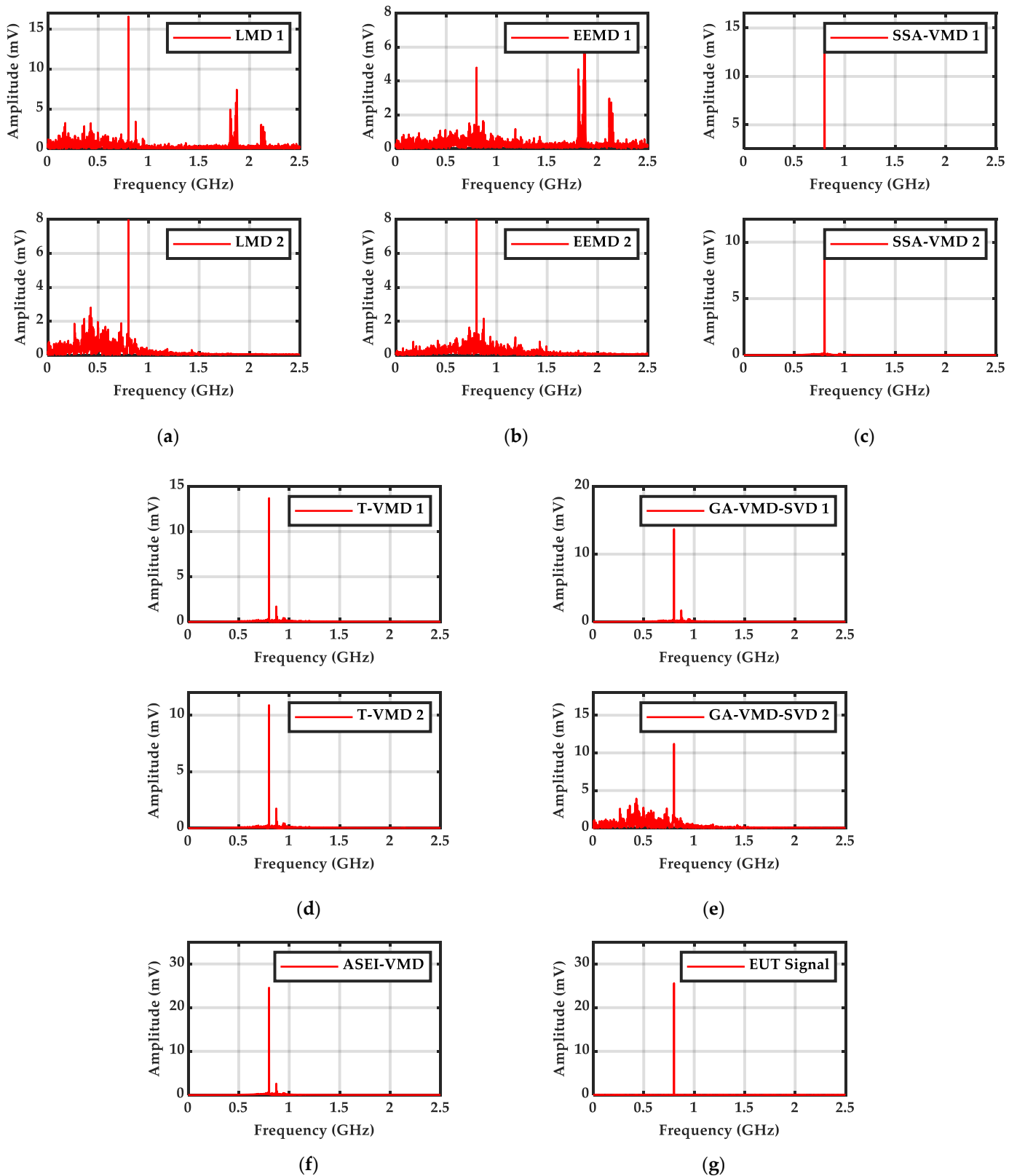
Figure 9. Comparison of actual measured results of the different decomposition methods: (**a**) the LMD; (**b**) the EEMD; (**c**) the SSA-VMD; (**d**) the T-VMD; (**e**) the GA-VMD-SVD; (**f**) the ASEI-VMD; (**g**) the actual EUT-radiated emission signals.
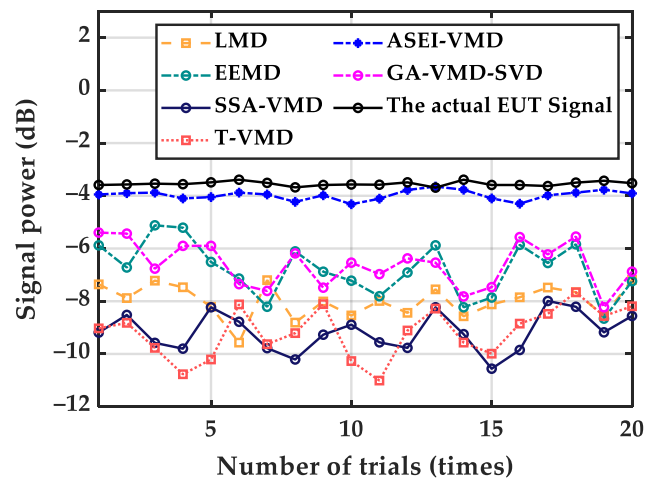
Figure 10. Comparison of EUT-radiated emission signal powers obtained by different signal decomposition methods.

4.2. Experimental Analysis of the Frequency-Domain Electromagnetic Interference Cancellation Method

After the IMF components carrying the EUT-radiated emission information within the two channels are identified, the electromagnetic interference present in the IMF components is effectively suppressed using a cancellation method. The ensuing content provides empirical evidence through experimental analysis to establish the validity of the proposed method in this paper.

Figure 11a is the experimental test's EUT-radiated emission signal mixed with environmental electromagnetic interference. Figure 11b shows the environmental electromagnetic interference mixed with a small amount of EUT-radiated emission signal collected by antenna B. Under the premise of ensuring the correlation of the background interference, it is impossible to avoid mixing the EUT-radiated emission signal in antenna B.
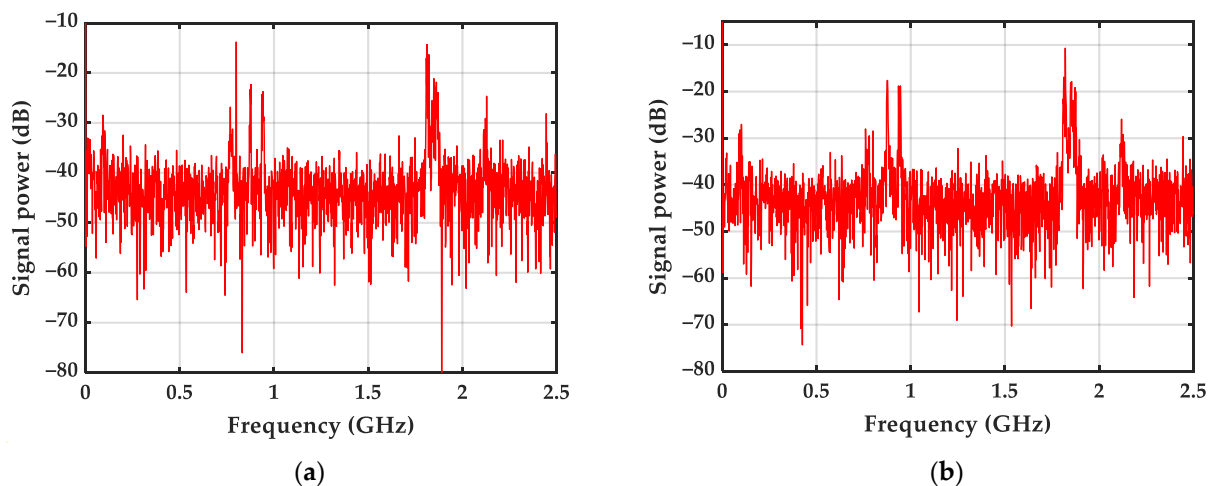
Figure 11. Comparison of the received signals in the two channels: (**a**) the received signals in antenna A; (**b**) the received signals in antenna B.

Figure 12a shows the error curve of the EUT-radiated emission powers and the actual EUT-radiated emission powers from 20 tests performed using the algorithm in this paper. Due to the continuous change of the field environment interference, the EUT-radiated emission power after each cancellation also changes. In the figure, both the 3 dB error line and the error curve obtained by the algorithm introduced in this paper are presented. It is

evident that the errors produced by the algorithm consistently remain below the threshold of 3 dB, thus confirming the efficacy of the approach proposed in this study.
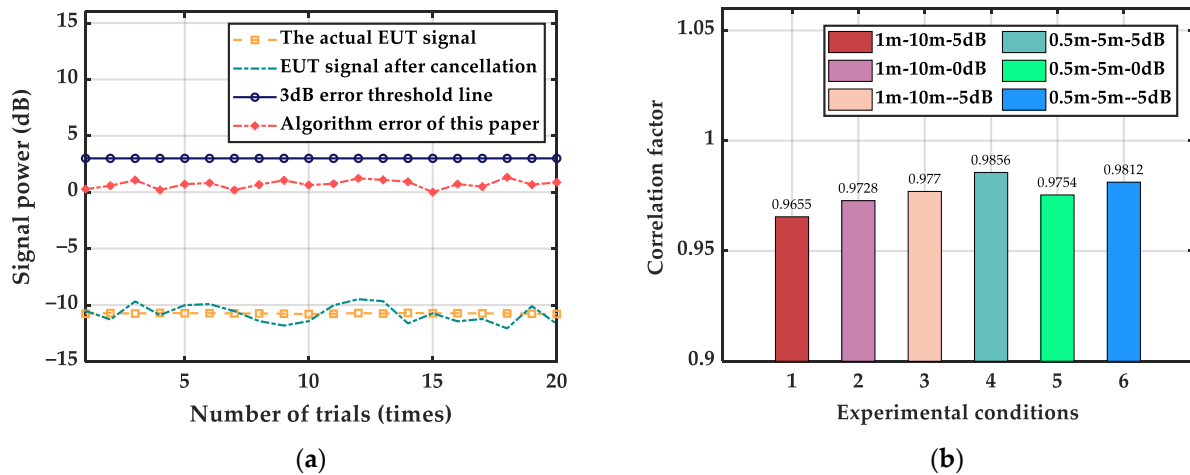
Figure 12. Results of the power errors and the correlation between the EUT-radiated emission signal after cancellation and the actual EUT-radiated emission signal obtained at different SIRs: (**a**) the comparison of power errors; (**b**) the comparison of correlation.

Figure 12b compares the correlation between the EUT-radiated emission signals obtained by the algorithm in this paper and the actual EUT-radiated emission signals under different test distances and emission powers (in Figure 12b, for A m-B m-C dB, A represents the distance from antenna A to the EUT-emitting antenna, B represents the distance from antenna B to the EUT emitting antenna, and C represents the signal powers emitted by the signal generator). The analysis of the figure shows that the correlation can reach more than 96%, and the interference error of the EUT-radiated emission signal is minimal. Even with a petite SIR at an emission power of −5 dB, the algorithm proposed in this paper can accurately extract the EUT-radiated emission signal. Thus, the effectiveness of the method in this paper is verified.

Table 2 describes the algorithm's cancellation performance across varying test distances and signal emission powers. The analysis in Table 2 indicates that variations in the distance between test antennas A and B impact the precision of the algorithm's cancellation performance. The correlation of their environmental interference increases as the distance between the two test antennas decreases; conversely, the correlation diminishes as the distance increases. Due to the constantly changing electromagnetic interference in the environment, its errors will also fluctuate up and down. Following numerous experiments and thorough comparisons, it has been established that the error of the algorithm proposed in this paper consistently remains below 3 dB, aligning with the practical testing requirements.

Table 2. Comparison of output power errors under different test conditions.

Signal Parameter Settings (A m—B m—C dB)	Actual EUT-Radiated Emission Power (dB)	EUT-Radiated Emission Power after Cancellation (dB)	Signal Power Error (dB)
0.5 m—5 m—5 dB	−5.163	−6.471	1.308
0.5 m—5 m—0 dB	−9.784	−10.773	0.989
0.5 m—5 m—−5 dB	−17.10	−17.14	0.04
1 m—10 m—5 dB	−4.47	−5.031	0.561
1 m—10 m—0 dB	−9.617	−9.155	0.462
1 m—10 m—−5 dB	−15.085	−14.096	0.989

In Table 2, the meanings represented by A, B, and C are the same as in Figure 12b.

5. Conclusions

This paper presents a novel frequency-domain electromagnetic interference cancellation approach leveraging the ASEI-VMD. The method is applied to test actual radiated emission peculiarities from the EUT within intricate electromagnetic environments. The problem of obtaining the actual EUT-radiated emission signal from a complex electromagnetic interference environment without prior knowledge is addressed. Here are the conclusions:

The *ASEER* is introduced as the objective function, employing an iterative approach that initially establishes the number of decomposition layers *K*, followed by the determination of the penalty factor α. The issues of over- and under-decomposition are avoided, and the challenge of inappropriate parameter selection resulting from the simultaneous increase of K and α is mitigated.

Compared with decomposition methods such as EEMD, LMD, T-VMD, GA-VMD-SVD, and SSA-VMD, ASEI-VMD excels in accurately and comprehensively extracting the IMF component containing EUT-radiated emission information. The ASEI-VMD exhibits both low computational complexity and exceptional stability.

The method in this paper applies to the scenario where the EUT-radiated emission signal is mixed into the remote antenna B. The EUT signal's strength of antenna B does not affect the algorithm's accuracy, which is unavoidable in the actual test environment.

This method has no strict requirements for the test environment and can effectively extract actual EUT-radiated emission signal without prior conditions. The correlation between the obtained EUT-radiated emission signal and the actual EUT-radiated emission signal is greater than 96%. The errors of the obtained signal power are below 3 dB. This method is suitable for conducting electromagnetic radiation emission testing in complex electromagnetic environments.

This paper mainly solves the problem of accurately extracting the EUT-radiated emission signal without prior knowledge and when both receiving antennas contain EUT radiation emission information. The extracted EUT-radiated emission signals conform to the testing requirements. The experimental design in this article primarily validates the narrow-band electromagnetic radiation emission test within a complex environment. In the future, we will verify whether the broadband electromagnetic radiation emission test conforms to the requirements. Simultaneously, we will address the challenge of mitigating co-channel interference, which is expected to be a significant undertaking.

Author Contributions: Conceptualization, D.C., M.J. and Q.F.; methodology, D.C. and W.L.; software, D.C., M.J. and Q.F.; validation, D.C., M.J. and W.L.; formal analysis, D.C.; investigation, J.L., D.C. and Q.F.; resources, M.J. and W.L.; data curation, D.C., M.J. and Q.F.; writing—original draft preparation, J.L., D.C., M.J. and W.L.; writing—review and editing, J.L., Q.F. and W.L.; supervision, W.L.; project administration, W.L; funding acquisition, W.L. All authors have read and agreed to the published version of the manuscript.

Data Availability Statement: Not applicable.

References

1. Kim, S.; Altinsoy, M. A Complementary Effect in Active Control of Powertrain and Road Noise in the Vehicle Interior. *IEEE Access.* **2022**, *10*, 27121–27135. [CrossRef]
2. Jin, M.; Wang, S.; Liu, S.; Fang, Q.; Liu, W. Statistical Study on the Time Characteristics of the Transient EMD Excitation Current from the Pantograph–Catenary Arcing Discharge. *Electronics* **2023**, *12*, 1262. [CrossRef]

3. Lu, H.; Zhang, Q. EMI effect of pantograph catenary arc of high-speed railway on aircraft approach landing. *Acta Aeronaut. Astronaut. Sin.* **2020**, *41*, 339–347. (In Chinese)

4. Zhou, Z.; Li, P.; Sheng, M.; Zhou, Q.; Hu, P. Ambient Interferences Suppressing for In-Situ Radiated Emissions Measurement Based on Array Signal Processing and Adaptive Noise Cancellation. *IEEE Trans. Electromagn. Compat.* **2020**, *62*, 1055–1067. [CrossRef]

5. Chang-Bin, H.; Baik, J.; Song, H. Successive Partial Interference Cancellation Scheme for FD-MIMO Relaying. *IEICE Trans. Fundam. Electron. Commun. Comput. Sci.* **2017**, *E100*, 1729–1732.

6. Ezilarasan, M.; Britto Pari, J.; Leung, M. Reconfigurable Architecture for Noise Cancellation in Acoustic Environment Using Single Multiply Accumulate Adaline Filter. *Electronics* **2023**, *12*, 810. [CrossRef]

7. Park, S.; Park, D. Low-Power FPGA Realization of Lightweight Active Noise Cancellation with CNN Noise Classification. *Electronics* **2023**, *12*, 2511. [CrossRef]

8. Usta, Z.; Doan, H. Speech protected noise cancellation system in noise dominated environments. *Appl. Acoust.* **2022**, *189*, 108577. [CrossRef]

9. Shen, J.; Lin, Z.; Huang, L.; Ruan, X.; Tang, F. A Low-Noise Analog Front End with Interstage Systematically Ambient Interference Cancellation for Pulse Oximeter. *Electronics* **2022**, *11*, 868. [CrossRef]

10. Al-Naggar, N.; Al-Udyni, M. Performance of Adaptive Noise Cancellation with Normalized Last-Mean-Square Based on the Signal-to-Noise Ratio of Lung and Heart Sound Separation. *J. Healthc. Eng.* **2018**, *2018*, 9732762. [CrossRef]

11. Remadevi, M.; Sureshkumar, N.; Rajesh, R.; Santhanakrishnan, T. Cancellation of Towing Ship Interference in Passive SONAR in a Shallow Ocean Environment. *Defence. Sci. J.* **2022**, *1*, 72.

12. Lu, Z.; Ding, L.; Lin, X. An Innovative Virtual Chamber Measurement Method Based on Spatial Domain Cancellation Technique for Radiation Emission in Situ Test. *IEEE Trans. Electromagn. Compat.* **2016**, *2*, 342–351. [CrossRef]

13. Lu, Z.; Liu, B.; Liu, P. A Novel Method of Ambient Interferences Suppressing for In Situ Electromagnetic Radiated Emission Test. *IEEE Trans. Electromagn. Compat.* **2012**, *54*, 1205–1215. [CrossRef]

14. Zhang, L.; Liu, S.; Li, B. The Study of an Improved Adaptive Interference Cancellation Technology and Its Application in the Electromagnetic Radiation Measurement. *Acta Electron. Sin.* **2011**, *39*, 1394–1398. (In Chinese)

15. Liu, S.; Wang, B.; Zhang, L. A Method for Blind Source Separation of Multichannel Electromagnetic Radiation in the Field. *IEEE Access.* **2020**, *8*, 191341–191354. [CrossRef]

16. Cakir, S.; Celep, M.; Sen, O. A New Approach to Background Noise Cancellation in Time Domain for Low-Frequency Emission Testing. *IEEE Trans. Electromagn. Compat.* **2019**, *99*, 1899–1910. [CrossRef]

17. Zhang, L.; Zhou, J.; Li, B.; Sun, B. Research on automatic noise spectral estimation suppression technique and its application. *J. Harbin Inst. Technol.* **2015**, *47*, 31–35. (In Chinese)

18. Dragomiretskiy, K.; Zosso, D. Variational Mode Decomposition. *IEEE Trans. Signal Process.* **2014**, *62*, 531–544. [CrossRef]

19. Zhang, P.; Gao, D.; Lu, Y.; Kong, L.; Ma, Z. Online chatter detection in milling process based on fast iterative VMD and energy ratio difference. *Measurement* **2022**, *194*, 194. [CrossRef]

20. Ding, J.; Huang, L.; Xiao, D.; Li, X. GMPSO-VMD Algorithm and Its Application to Rolling Bearing Fault Feature Extraction. *Sensors* **2020**, *20*, 1946. [CrossRef]

21. Wei, X.; Feng, G.; Qi, T.; Guo, J.; Li, Z.; Zhao, D.; Li, Z. Reduce the Noise of Transient Electromagnetic Signal Based on the Method of SMA-VMD-WTD. *IEEE Sens. J.* **2022**, *22*, 14959–14969. [CrossRef]

22. Mei, L.; Li, S.; Zhang, C.; Han, M. Adaptive Signal Enhancement Based on Improved VMD-SVD for Leak Location in Water-Supply Pipeline. *IEEE Sens. J.* **2021**, *21*, 24601–24612. [CrossRef]

23. Li, Z.; Lv, Y.; Yuan, R.; Zhang, Q. An Intelligent Fault Diagnosis Method of Rolling Bearings via Variational Mode Decomposition and Common Spatial Pattern-Based Feature Extraction. *IEEE Sens. J.* **2022**, *22*, 15169–15177. [CrossRef]

24. Mao, J.; Li, Z.; Li, S.; Li, J. A Novel ECG Signal Denoising Algorithm Based on Sparrow Search Algorithm for Optimal Variational Modal Decomposition. *Entropy* **2023**, *25*, 775. [CrossRef] [PubMed]

25. Li, Y.; Tang, B.; Jiang, X.; Yi, Y. Bearing Fault Feature Extraction Method Based on GA-VMD and Center Frequency. *Math. Probl. Eng.* **2022**, *2022*, 2058258. [CrossRef]

26. Wang, C.; Li, H.; Huang, G.; Ou, J. Early Fault Diagnosis for Planetary Gearbox Based on Adaptive Parameter Optimized VMD and Singular Kurtosis Difference Spectrum. *IEEE Access.* **2019**, *7*, 31501–31516. [CrossRef]

27. Li, H.; Liu, T.; Wu, T.; Li, S. Correlated SVD and Its Application in Bearing Fault Diagnosis. *IEEE Trans. Neural Netw. Learn. Syst.* **2023**, *34*, 355–365. [CrossRef]

28. Wang, Q.; Wang, L.; Yu, H.; Wang, D.; Nandi, A.K. Utilizing SVD and VMD for Denoising Non-Stationary Signals of Roller Bearings. *Sensors* **2022**, *22*, 195. [CrossRef]

29. Guo, M.; Wu, Z. Noise Reduction for High-Accuracy Automatic Calibration of Resolver Signals via DWT-SVD Based Filter. *Electronics* **2019**, *8*, 516. [CrossRef]

30. Li, Y.; Si, S.; Liu, Z.; Liang, X. Review of local mean decomposition and its application in fault diagnosis of rotating machinery. *J. Syst. Eng. Electron.* **2019**, *30*, 799–814.

31. Sheng, A.; Xie, Y.; Zhou, Y.; Wang, Z.; Liu, Y. A Hybrid Model Based on Complete Ensemble Empirical Mode Decomposition with Adaptive Noise, GRU Network and Whale Optimization Algorithm for Wind Power Prediction. *IEEE Access.* **2023**, *11*, 62840–62854. [CrossRef]